Deterministic 1D Domain Wall Motion with Nucleation-Free Nature in Sliding Ferroelectric Switching

Jiangang Chen,[1,*] Changming Ke,[2,3,*] Renji Bian,[1,*] Er Pan,[1,*] Peter Kun,[4] Zefen Li,[1] Biao Dong,[1,5]
Fan Yang,[1] Qing Liu,[1] Levente Tapaszto,[4] Xiao Luo,[1,†] Shi Liu,[2,3,‡] and Fucai Liu[1,6,§]
[1]*School of Optoelectronic Science and Engineering, University of Electronic Science and Technology of China, Chengdu, 611731, China*
[2]*Department of Physics, School of Science, Westlake University, Hangzhou, 310030, China*
[3]*Institute of Natural Sciences, Westlake Institute for Advanced Study, Hangzhou, 310024, China*
[4]*Hungarian Research Network, HUN-REN Centre for Energy Research, Institute of Technical Physics and Materials Science, 1121 Budapest, Hungary*
[5]*School of Physics, Nankai University, Tianjin, China*
[6]*State Key Laboratory of Electronic Thin Films and Integrated Devices, University of Electronic Science and Technology of China, Chengdu, China*

(Received 21 May 2025; accepted 17 February 2026; published 26 March 2026)

Inhomogeneous domain nucleation and stochastic motion of the domain wall (DW) during the polarization switching process in conventional ferroelectrics introduce a spectrum of intricate kinetic challenges for the reliable and precise manipulation of polarization states, a prerequisite for many ferroelectric implementations. Combining deep-learning-assisted molecular dynamics simulations, microscopic-scale *in situ* observations, and device-scale electrical measurements, it reveals that sliding ferroelectrics inherently circumvent these issues, with an intrinsic domain-nucleation-free polarization reversal. Using $3R$-MoS_2 as a model system, we demonstrate that DW motion occurs along a well-defined 1D pathway in a collective manner, without domain nucleation. Leveraging this predictable domain dynamics, we demonstrate deterministic multistate polarization switching, achieving remarkable precision and repeatability with a variation coefficient of less than 0.2%, 10 times improved over conventional ferroelectrics. This work provides valuable insights into the unique kinetics of DW motion in sliding ferroelectrics and offers opportunities for ferroelectric multistate devices with ultraprecision control.

DOI: 10.1103/q624-x397 Subject Areas: Condensed Matter Physics

I. INTRODUCTION

Driven by the growing demand for high-density data storage in fields such as neuromorphic devices [1,2] and multibit storage devices [3,4], ferroelectrics with switchable spontaneous polarization have attracted significant interest. To achieve reliable multistate modulation, precise control over domain wall (DW) motion is essential [5]. However, ferroelectricity typically involves complex domain-nucleation processes [whether homogeneous or inhomogeneous [6], as illustrated in Fig. 1(a)], which are driven by thermodynamic fluctuations and are inherently stochastic [5,7,8]. This mechanism results in the nonlinear creep of DWs, even under defect-free conditions [9]. Consequently, ferroelectric polarization switching behavior often manifests in multiple, unpredictable forms [Fig. 1(b)], making it a probabilistic system characterized by distributions [10–13]. Defects with local variations further exacerbate this response [14–16], leading to significant overlap in the polarization response of multiple programmable states and rendering them practically indistinguishable [17] [Fig. 1(c)].

Distinct from the ion-displacement-induced polarization in conventional ferroelectrics, sliding ferroelectrics were recently proposed and observed at the symmetry-broken van der Waals interface, where the spontaneous polarization arises from interlayer charge redistribution [18–20]. The polarization switching in sliding ferroelectricity involves the collective motion of atomic layers along the in-plane direction, perpendicular to the switching field [21–24]. Such a collective dipole reversal occurring at the level of layer structures rather than unit cells makes sliding

---

[*] These authors contributed equally to this work.
[†] Contact author: luox@uestc.edu.cn
[‡] Contact author: liushi@westlake.edu.cn
[§] Contact author: fucailiu@uestc.edu.cn

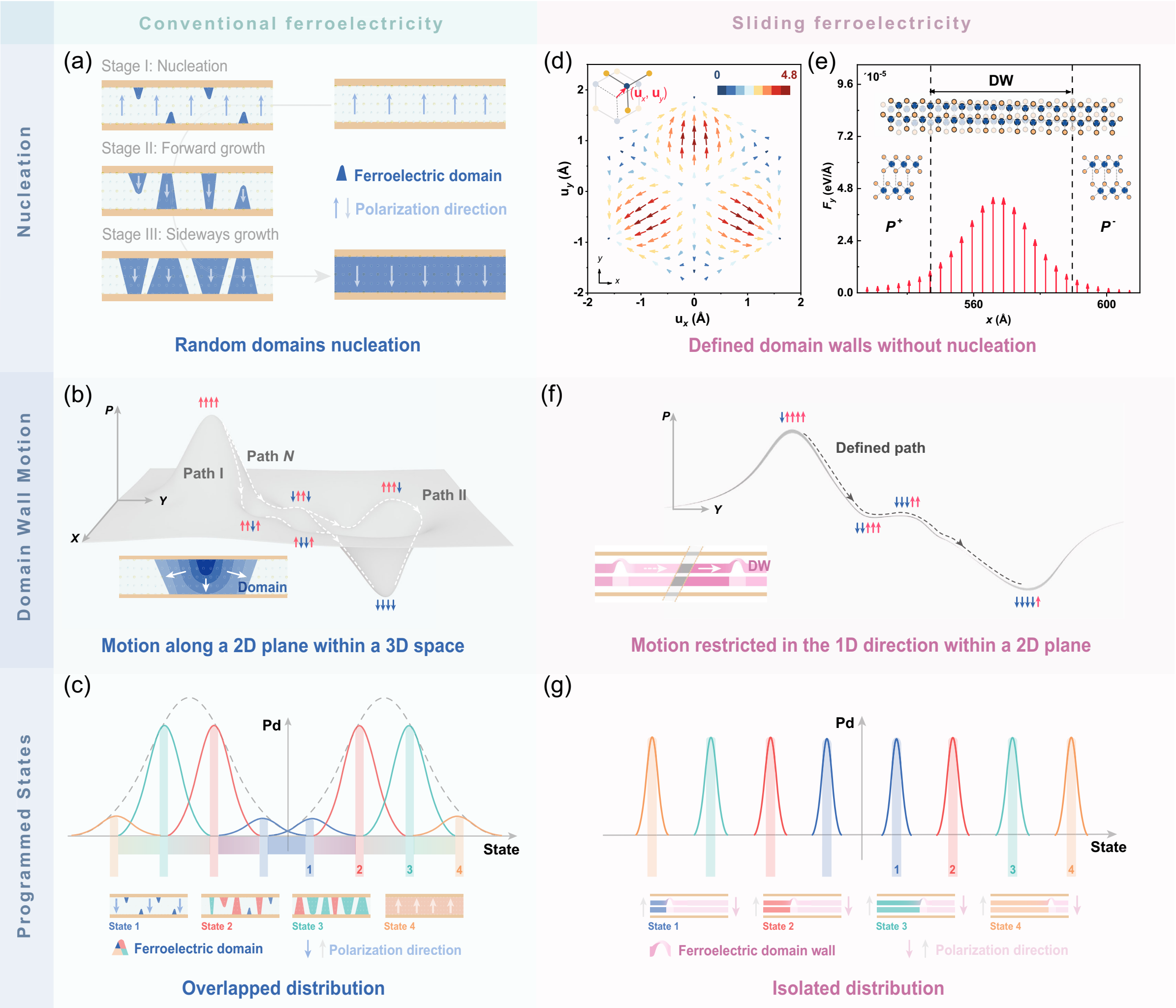

FIG. 1. Schematic diagram comparing conventional ferroelectricity with sliding ferroelectricity in domain nucleation, DW motion, and programmed states. (a) Schematic diagram of domain nucleation in the polarization reversal process of conventional ferroelectricity. (b) Schematic diagram of DW motion in conventional ferroelectricity. The schematic diagram in the lower left corner shows the growth process of a single domain. The red and blue arrows represent upward and downward polarizations, respectively. The white dashed lines and arrows represent the possible paths and directions of DW motion, respectively. (c) Schematic diagram of overlapped programmable state distributions with corresponding domain configurations in conventional ferroelectricity. (d) Calculated distribution of the in-plane force acting on the unit cell in the top layer as a function of the displacement vector $(\mathrm{u}_x, \mathrm{u}_y)$ under a 0.3 V/nm out-of-plane electric field ($E_{\mathrm{OP}} = 0.3\ \mathrm{V/nm}$). Each arrow represents the calculated in-plane force vector for a specific bilayer configuration and is color coded to indicate force magnitude (color scale in the upper right inset). Counterintuitively, the in-plane force is strictly zero in both AB- and BA-stacking configurations responsible for the domain-nucleation-free feature in sliding ferroelectrics. The inset in the upper left corner defines the in-plane displacement vector $(\mathrm{u}_x, \mathrm{u}_y)$. (e) Profile of the unit-cell in-plane forces (F_y) in the top layer induced by $E_{\mathrm{OP}} = 0.3\ \mathrm{V/nm}$. Only unit cells near the domain wall experience collective in-plane forces along the y axis. Each arrow represents the calculated in-plane force vector for a specific bilayer configuration containing a DW. The top inset shows a schematic of a Σ_0-type wall separating the downward polarization P^- domain (the right inset) with $(\mathrm{u}_x, \mathrm{u}_y) = (0, 0)$ and the upward polarization P^+ domain (the left inset) with $(\mathrm{u}_x, \mathrm{u}_y) = (\mathrm{u}_0, 0)$. The wall extends along the y axis and is parallel to the displacement vector $(\mathrm{u}_x, \mathrm{u}_y)$. (f) Schematic diagram of DW motion in sliding ferroelectricity. The schematic diagram in the lower left corner shows the motion process of a single domain wall. The red and blue arrows represent upward and downward polarizations, respectively. The gray dashed lines and arrows represent the path and direction of domain wall motion, respectively. (g) Schematic diagram of isolated programmable state distributions with corresponding domain configurations in sliding ferroelectricity.

ferroelectrics potentially more robust against thermal and defective fluctuations [25,26]. Using the prototypical sliding ferroelectric 3R-MoS$_2$, we studied in detail the polarization switching process through molecular dynamics (MD) simulations. We identified that the tensorial properties of Born effective charges (BECs) play a crucial role in generating in-plane driving forces when an out-of-plane electric field is applied [Fig. 1(d)]. Notably, only atoms located at DWs, which break the C_3 symmetry, exhibit nonzero off-diagonal BEC elements. This enables the creation of net in-plane forces that facilitate DW motion [Fig. 1(e)]. Unlike conventional ferroelectrics (e.g., $CuInP_2S_6$, α-In_2Se_3 [27,28]), where atoms in both domains and DWs respond to external electric fields, sliding ferroelectrics restrict switching to atoms near DWs, leaving those within the domains unaffected. As a result, polarization reversal in sliding ferroelectrics is governed by DW motion and involves only local atomic displacements rather than global interlayer shifts in domains hypothesized previously, thus strictly prohibiting domain nucleation. These unique characteristics are confirmed by deep-potential molecular dynamics (DPMD; see Sec. V, Supplemental Material Figs. S1–S3 [29], and Refs. [30,31] for details.) simulations combined with a local atomic environment-dependent BEC model that captures dynamic charge transfer during DW motion, as detailed in Supplemental Material Figs. S4 and S5 [29].

This domain-nucleation-free property in sliding ferroelectrics allows the control of polarization switching to shift entirely to DW motion, thereby defining a new paradigm, “no domain wall, no polarization reversal,” that is fundamentally distinct from conventional ferroelectric switching. Interestingly, as shown in Fig. 1(f), DW motion is inherently restricted to a one-dimensional (1D) path within a two-dimensional (2D) atomic plane. This confinement significantly reduces the stochasticity observed in conventional ferroelectrics, where DW motion often follows complex pathways [Fig. 1(b)]. Moreover, the inevitable imperfect factors [32] during device fabrication, such as bubbles, or edges of the sample, introduce additional energy barriers, further constraining DW motion. These factors ensure that the polarization reversal is dominated by predictable switching dynamics, enabling well-defined programmable states [Fig. 1(g)].

Here, we systematically investigate DW motion in sliding ferroelectrics through MD simulations, microscopic-scale *in situ* observations, and device-scale electric-field scanning. We revealed that DW motion is collective, inherently constrained, and free from domain-nucleation processes. Meanwhile, the involvement of pinning sites enables the coexistence of both deterministic and stochastic behaviors. On this basis, we achieved precise control over DW motion. Our devices exhibit exceptional ferroelectric multistate modulation, with a coefficient of variation between 0.1% and 0.2%, limited solely by measurement noise level. The structurally constrained nature of sliding ferroelectrics allows us to focus exclusively on precisely controllable DW motion, unlocking unprecedented opportunities for building reliable memory architectures, ultrasensitive sensors, and next-generation computing paradigms based on structural phase transitions.

II. RESULTS

To directly observe the DW motion at the microscopic scale, we conducted Kelvin probe force microscopy (KPFM) characterization [33]. As shown in Fig. 2 (with corresponding height images in Supplemental Material Fig. S6 [29]), clear domains (orange and purple regions) with distinct surface potentials corresponding to AB- and BA-stacked configurations are observed, separated by narrow DWs. We applied a local electric field via the tip voltage to spatially control the polarization switching for tracking DW dynamics. By applying a positive tip voltage, the size of the BA domains increased, accompanied by a reduction in the size of the AB domains and the movement of the DW separating them. Notably, we exclude tip-induced artifacts in domain imaging and demonstrate that repeated dc bias within a single domain induces no DW motion, whereas a single dc bias at the wall readily drives domain expansion or contraction (see Supplemental Material Figs. S7 and S8 [29]). These observations confirm that polarization switching is dominated by DW motion, thus motivating our focus on DW dynamics.

As shown in Fig. 2(a), after applying a 3.5-V probe voltage to the $3R$-MoS_2 sample, the movement of the DW was constrained upon encountering a bubble as a pinning site, resulting in localized deformation with inward curvature. However, when a higher voltage (5 V) was applied,

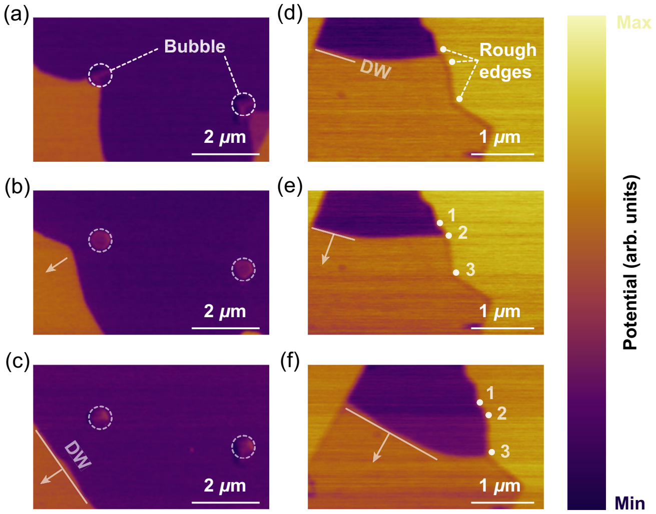

FIG. 2. KPFM characterization of $3R$-MoS_2 samples. (a)–(c) Surface potential images of $3R$-MoS_2 samples with bubbles measured after applied voltages of 3.5 V (a), 5 V (b), and back to 3.5 V (c), respectively. The dotted circles mark the location of the bubble. The white straight lines indicate the DW, and the arrows represent the direction of DW motion. (d)–(f) Surface potential images of $3R$-MoS_2 samples with rough edges measured after applied voltages of 1 V (d), 2 V (e), and 3 V (f), respectively. The white dots in (d) and the numbers in (e) and (f) mark the pinning sites at the rough edges. The white straight lines indicate the DW, and the arrows represent the direction of the DW motion.

the DW traversed the bubble, undergoing only slight deformation without splitting [Fig. 2(b)]. Upon reducing the voltage back to 3.5 V, the DW continued to move, and its morphology reverted to the expected straight configuration (the lowest-energy state) [34], as shown in Fig. 2(c). We attribute this curvature to local pinning at the mesoscopic defect site, while the remaining segments of the domain wall retain nearly superlubric motion in the sliding ferroelectric. Notably, although lacking temporal resolution, KPFM unambiguously reveals nucleation through the spatial emergence of new domains. Indeed, no nucleation of oppositely polarized domains was observed throughout our measurements, even after multiple dc bias cycles applied within single-domain regions containing atomic-scale defects (see Supplemental Material Figs. S9 and S10 [29]), consistent with our MD simulations. Furthermore, we observed that the displacement vector was consistently perpendicular to its DW line, even after repeated pinning and depinning processes from the pinning sites at the rough edges [Figs. 2(d)–2(f)]. This also aligns with our simulations, as in sliding ferroelectrics, atoms need to slide along a kinetically favorable path to form stacked domains.

In situ observation of DW motion reveals that it occurs collectively along a specific 1D direction within a confined 2D atomic plane. To understand this inherently constrained property through the switching behavior in ferroelectric devices, we fabricated a dual-gate field-effect transistor [Fig. 3(a)] based on bilayer $3R$-MoS$_2$ and performed systematic electrical measurements. The corresponding

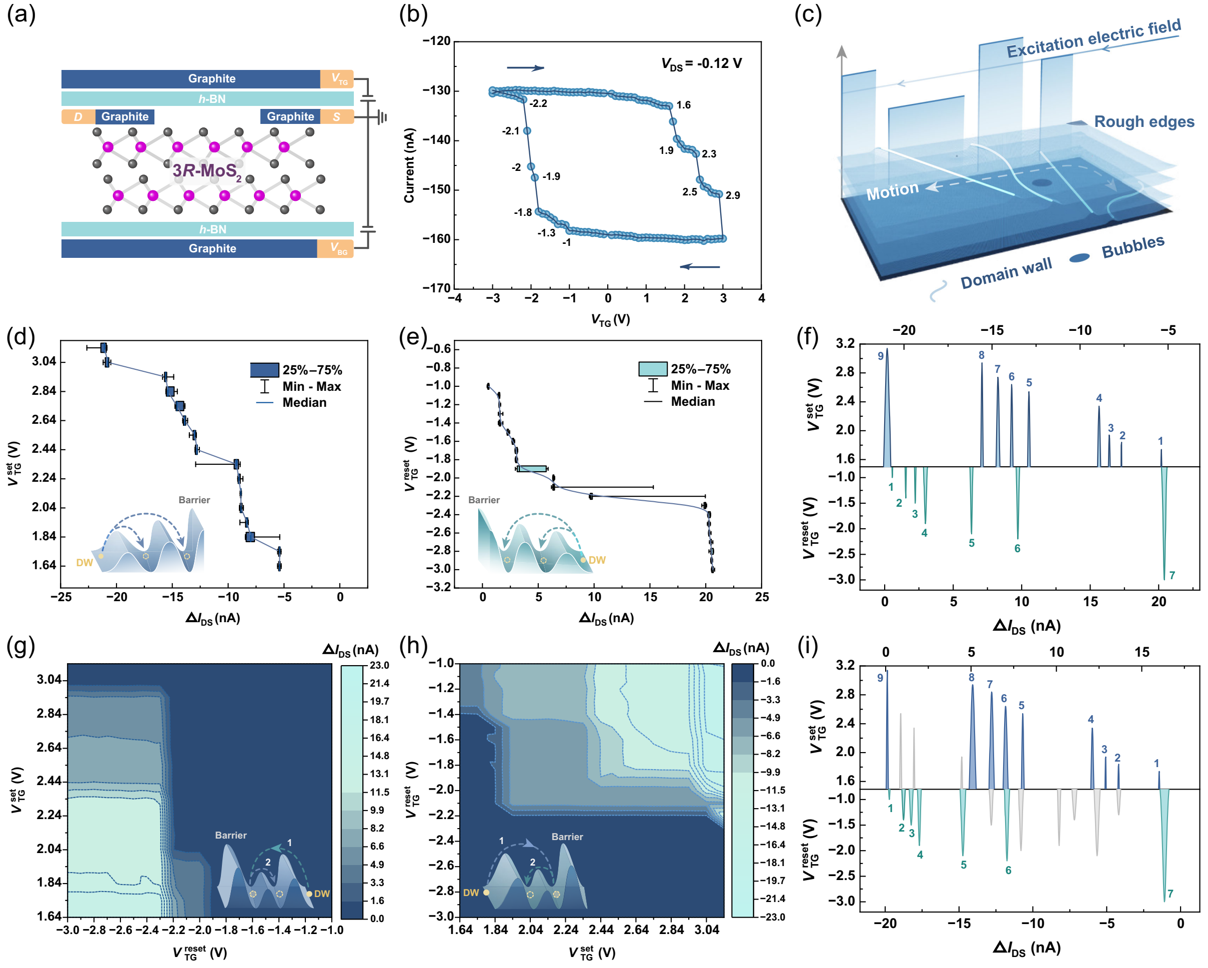

FIG. 3. Electrical scanning of the DW motion pathway in the $3R$-MoS$_2$ dual-gate device. (a) Schematic of a typical bilayer $3R$-MoS$_2$ dual-gate device. (b) Typical rectangular hysteresis loop obtained from static electrical measurements. (c) Schematic of the DW motion pathway scanned by an electric field. (d),(e) Box plot illustrates the distribution characteristics of ΔI_{DS} obtained from the forward (d) and backward (e) sequential scanning measurements, as depicted in the inset, with the dashed arrows indicating the DW trajectories during the application of V_{TG}^{set} (d) or V_{TG}^{reset} (e). The curve connects the medians of each group in the box plot. (f) Energy barrier profiles with assigned amplitudes obtained from the Lorentzian function fitting within each data interval in (d) and (e). (g),(h) Mapping image of ΔI_{DS} obtained from the forward (g) and backward (h) iterative scanning measurements, as depicted in the inset, with the dashed arrows indicating the application of V_{TG}^{reset} and V_{TG}^{set} (g) or V_{TG}^{set} and V_{TG}^{reset} (h) sequentially. (i) Energy barrier profiles with assigned amplitudes obtained from the Lorentzian function fitting within each data interval in (g) and (h).

optical micrographs and material characterization (see Sec. V for details) are presented in Supplemental Material Fig. S11 [29]. The typical transistor electrical characteristics, including the output and transfer curves, along with the ferroelectricity confirmed through dynamic electrical measurements, are presented in Supplemental Material Fig. S12 (see Note 1 in Supplemental Material [29] for a detailed discussion).

The electrical measurement curve from static electrical measurements (see Sec. V and Supplemental Material Fig. S13 [29] for details) exhibits a typical rectangular hysteresis loop [Fig. 3(b)] with stepwise evolution in the drain current. Since the polarization switching occurs through DW motion [19], we attribute this stepwise behavior to the DW motion overcoming successive energy barriers (primarily induced by pinning sites) [35]. The pulse-width-dependent switching measurement (see Supplemental Material Fig. S14 [29]) further demonstrates that each energy barrier has a determinable potential energy (as these steps consistently occur under fixed electric fields) and rules out the possibility that charge trapping causes those steps (which exhibits significant time correlation [24]). Moreover, no evidence of nucleation-and-growth dynamics [6,36] was observed in the switching kinetics measurements within the experimentally accessible pulse-width window (20 ns to 1 s; see Supplemental Material Fig. S15 [29]). The above results indicate that by identifying both the strength (indexed by V_{TG}) and the site (correlated with I_{DS}) of the energy barriers restricting DW motion, we can trace their distribution during ferroelectric switching, thus revealing the DW motion pathways [Fig. 3(c)]. Therefore, we performed V_{TG}-V_{BG} sequential scanning measurements to identify the main energy barriers (the configurations of measurements are detailed in Sec. V). Here, ΔI_{DS} is defined as the difference between the drain currents measured after applying gate voltage excitation pulses $V_{\mathrm{TG}}^{\mathrm{set}}$ or $V_{\mathrm{TG}}^{\mathrm{reset}}$, and their corresponding revert pulses $V_{\mathrm{TG}}^{\mathrm{revert}}$ (the definitions of ΔI_{DS}, $V_{\mathrm{TG}}^{\mathrm{set}}$, $V_{\mathrm{TG}}^{\mathrm{reset}}$, and $V_{\mathrm{TG}}^{\mathrm{revert}}$ are detailed in Supplemental Material Fig. S16 [29]). The statistics of ΔI_{DS} obtained from forward and backward scans are shown in Figs. 3(d) and 3(e), respectively. We divided the potential intervals based on the multimodal distribution of ΔI_{ds} and performed Lorentzian function fitting within each interval (see Sec. V, and Note 2 and Fig. S17 in Supplemental Material [29] for details), establishing the relationship between $V_{\mathrm{TG}}^{\mathrm{set}}$, $V_{\mathrm{TG}}^{\mathrm{reset}}$, and ΔI_{ds}, as shown in Fig. 3(f). Multiple distinct and well-separated peaks indicate that these energy barriers fragment DW motion into a series of isolated processes, dominating it along a well-defined pathway. This result indicates that the switching behavior in sliding ferroelectric devices is largely predictable and repeatable. In contrast, conventional ferroelectrics, when strongly affected by local variations of free energy, exhibit a highly inhomogeneous process with complex kinetics [37].

To reveal the complete potential pathways of DW motion and to further evaluate its precision, we performed iterative scanning measurements (the configurations of measurements and the definitions of ΔI_{DS}, $V_{\mathrm{TG}}^{\mathrm{set}}$, $V_{\mathrm{TG}}^{\mathrm{reset}}$, and $V_{\mathrm{TG}}^{\mathrm{revert}}$ are detailed in Sec. V and Supplemental Material Fig. S18 [29]) to map the energy barrier landscape. The ΔI_{DS} obtained after forward [Fig. 3(g)] and backward [Fig. 3(h)] scans exhibits clear and regular color levels, indicating that DW motion is constrained to a specific pathway rather than occurring randomly between energy barriers. Similarly, after dividing the intervals according to the histogram distribution, a Lorentzian function was used to fit ΔI_{DS} within each interval (see Sec. V, and Note 2 and Fig. S19 in Supplemental Material [29] for details) to establish the relationship between $V_{\mathrm{TG}}^{\mathrm{set}}$, $V_{\mathrm{TG}}^{\mathrm{rese}t}$, and ΔI_{DS} [Fig. 3(i)]. As expected, it uncovers additional weak energy barriers (the gray Lorentzian fits) between strong ones, which may be bypassed due to the inertial motion of DWs under high driving forces (see Supplemental Material Fig. S20 [29]), especially in amplitude-based sequential scanning measurements.

Notably, regardless of scanning direction (forward or backward) or form (sequential or iterative), the strengths and relative positions of those main energy barriers remain nearly consistent in Figs. 3(i) and 3(f). This observation suggests that DW motion is constrained to a highly robust and well-defined pathway, enabling it to sequentially encounter fixed energy barriers in 2D space along a specific 1D direction. This further suggests that pinning sites in sliding ferroelectrics provide a deterministic energy landscape that renders DW pathways trackable, predictable, and even tailorable. Therefore, the key to more controllable ferroelectric switching may not be more perfect samples, but indeed the opposite, with additional energy barriers ensuring more consistent, predictable switching dynamics.

Interestingly, the presence of energy barriers leads to the coexistence of both deterministic and stochastic behaviors in DW motion, as shown in Supplemental Material Fig. S21 [29]. For stochastic behaviors (where the standard deviation is much larger than 200 pA), the observed current fluctuations are typically "restricted" between two neighboring energy barrier sites, as illustrated by the box plot data for $V_{\mathrm{TG}}^{\mathrm{set}}$ at 1.84 and 2.34 V [Fig. 3(d)] and $V_{\mathrm{TG}}^{\mathrm{reset}}$ at -1.9 and -2.2 V [Fig. 3(e)]. Since thermally activated depinning constitutes a nonequilibrium critical phenomenon with inherently probabilistic dynamics [38], the observed behavior can be reasonably attributed to the nonsmooth DW motion caused by successive pinning and depinning events. Furthermore, a finer electric-field scan reveals that depinned domain walls exhibit stochastic yet controllable dynamics, as the switching probability increases with field strength (see Supplemental Material Fig. S22 [29]). In contrast, when the applied electric field is insufficient to overcome a barrier, the DW is confined and thus maintains a relatively definite position. This deterministic behavior (with a standard deviation less than 200 pA) indicates that DW motion can be precisely controlled by leveraging its pinning-depinning dynamics.

The deterministic behavior of DW motion offers a promising opportunity to achieve deterministic multistate polarization in ferroelectric devices. Therefore, it is necessary to tailor the amplitude of the V_{TG}-V_{BG} pulse to bypass nonsmooth barrier sites, ensuring deterministic polarization switching along with sufficient, linearly distributed ferroelectric intermediate states.

To verify the precise control of DW motion, we employed two modulation schemes: stepwise switching and direct switching. Stepwise switching relies on fine-tuned pulse trains to enhance DW motion control, as commonly applied in conventional ferroelectric devices [39,40]. Direct switching aims to precisely create any predefined polarization state without requiring a stepwise process. This approach places higher demands on the consistency and accuracy of DW motion under any given electric field, posing a challenge for conventional ferroelectrics [13].

In stepwise switching, the device current demonstrates stable and uniform rising and falling over 1000 cycles of excitation (V_{TG}-V_{BG} pulse settings are detailed in Supplemental Material Fig. S23 [29]), as shown in Fig. 4(a). Similarly, during 1760 cycles of direct switching (V_{TG}-V_{BG} pulse settings are detailed in Supplemental Material Fig. S24 [29]), the device can be precisely positioned from its initial state to any of nine distinct states with good retention (see Supplemental Material Fig. S25 [29]), as shown in Fig. 4(b). The close overlap of data points at each intermediate state in Figs. 4(a) and 4(b) demonstrates highly reproducible ferroelectric polarization programming. We further qualitatively visualized these schemes by applying a Gaussian probability density function to fit the data [41–43], demonstrating that

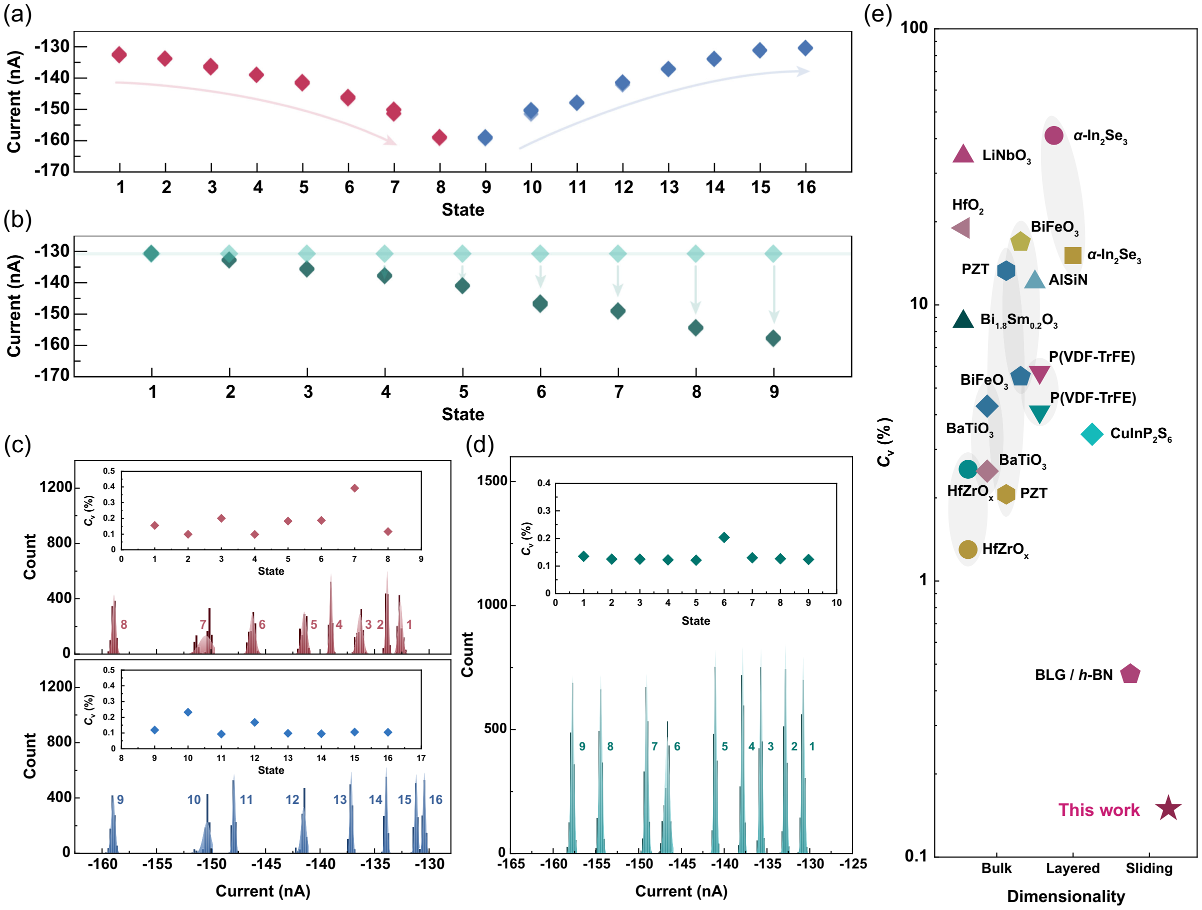

FIG. 4. Deterministic multistate polarization switching in the 3*R*-MoS$_2$ dual-gate device. (a) Performance of stepwise switching over 1000 cycles. (b) Performance of direct switching over 1760 cycles. (c),(d) Histograms of the raw data from (a) and (b) with corresponding illustrative Gaussian probability-density-function fits. The inset shows the coefficient of variation for different polarization states. (e) Benchmarking of polarization state variation reported in this work (shown as a five-pointed star) versus recently reported ferroelectricity-based devices (shown as other symbols). The data were deduced from LiNbO$_3$ [45], HfO$_2$ [46], Bi$_{1.8}$Sm$_{0.2}$O$_3$ [47], HfZrO$_x$ [40,48], BaTiO$_3$ [49,50], PZT [41,50], BiFeO$_3$ [51,52], AlScN [53], P(VDF-TrFE) [41,54], α-In$_2$Se$_3$ [39,55], CuInP$_2$S$_6$ [56], and BLG/*h*-BN [57].

the drain current distributions for different polarization states were highly concentrated, as shown in Figs. 4(c) and 4(d). As a well-established metric for cycle-to-cycle variability, the coefficient of variation (C_{v}) objectively quantifies programming consistency independent of absolute conductance levels [3,44]. Calculating the C_{v} from the experimental means and standard deviations, we found C_{v} values consistently between 0.1% and 0.2%, regardless of the modulation form. Notably, the variation is limited only by the measurement setup, because the standard deviation for different ferroelectric states has already approached the levels of their overall noise (see Supplemental Material Fig. S26 [29]).

Indeed, compared to bulk ferroelectric materials (e.g., $\mathrm{BaTiO_3}$ [49,58], $\mathrm{HfZrO_x}$ [40,45,48], $\mathrm{LiNbO_3}$ [45], and PZT [41,50]), van der Waals layered ferroelectric materials (e.g., α-$\mathrm{In_2Se_3}$ [39,55] and $\mathrm{CuInP_2S_6}$ [56]), and even Moiré ferroelectric materials (bilayer graphene/hexagonal boron nitride [BLG/h-BN], twisted two-dimensional heterostructures with specific periodic structures [57]), our devices exhibit exceptional polarization switching precision (the coefficient of variation is more than 10 times lower), as shown in Fig. 4(e). Importantly, this deterministic behavior is an intrinsic property of sliding ferroelectrics, rather than sample-specific artifacts (see Supplemental Material Fig. S27 [29]). Moreover, our devices exhibit excellent endurance, long-term temporal stability, and robustness against environmental charge noise (see Supplemental Material Figs. S28 and S29 [29]). This underscores that DW motion in bilayer $3R$-$\mathrm{MoS_2}$, as a unique domain kinetic process, offers an ideal platform for deterministic ferroelectric multistate control compared to those relying on the introduction of external factors to gain more control over the domain-nucleation process [59].

III. DISCUSSION

Our findings demonstrate that sliding ferroelectrics, exemplified by the bilayer $3R$-$\mathrm{MoS_2}$ model, exhibit domain-nucleation-free and highly predictable polarization reversal dynamics. Interestingly, the presence of pinning sites not only enhances the control of DW motion but also enables the coexistence of deterministic and stochastic behaviors. Although we have successfully achieved precise and stable multistate polarization modulation in deterministic behaviors, stochastic behaviors remain an area for further exploration. This "restricted" stochasticity is expected to unlock unique applications in electronic devices, particularly in algorithms such as random forests [60], Markov processes [61], genetic algorithms [62], and Bayesian optimization [63]. More fundamentally, constrained switching in sliding ferroelectrics is rooted in intrinsic structural properties rather than extrinsic stabilization mechanisms of conventional ferroelectrics [64,65]. Overall, we contend that the highly precise and predictable domain wall motion in sliding ferroelectrics reshapes the conventional understanding of ferroelectric polarization switching as a probabilistic process. Combining with the intriguing physical properties underlying the DW, this property positions sliding ferroelectrics as an ideal platform for investigating the structure-coupled novel physical properties [25], including magnetism, excitonic behavior, nontrivial topology, valley electronics, and superconductivity.

IV. CONCLUSIONS

In summary, we reveal that domain wall motion in sliding ferroelectrics is a collective, inherently constrained, and entirely nucleation-free process, confined to a 1D direction within the 2D atomic plane and following a robust, well-defined pathway. Building on this finding, we successfully achieve multiple precisely defined (with $< 0.2\%$ variation) and distinguishable polarization states by strictly controlling domain wall motion. This is distinct from the random nucleation-dominated process commonly observed in conventional ferroelectrics and provides opportunities for deterministic neuromorphic computing programming.

V. METHODS

A. Device fabrication

The chemical-vapor-transport method was adopted to grow the bulk $3R$-$\mathrm{MoS_2}$. The hexagonal boron nitride (h-BN) and graphite were supplied by HQ Graphene and NGS company, respectively. The $3R$-$\mathrm{MoS_2}$, h-BN, and graphite thin flakes were exfoliated on the silicon substrates covered with 285-nm $\mathrm{SiO_2}$. The thickness was verified by atomic force microscopy. Then, the flakes were picked up successively following the device structure with a poly (bisphenol A carbonate) film polydimethylsiloxane stamp at 90 °C. After removing the polymer in chloroform, the Cr and Au (8 and 50 nm, respectively) electrodes were introduced on the specific area in the device by metal e-beam evaporation. Finally, the device was annealed in a mixed $\mathrm{Ar/H_2}$ (9∶1) atmosphere at 100 sccm and 300 °C for 6 h to reduce the bubbles. Graphene contacts, h-BN dielectrics, and a dual-gate architecture were employed to ensure a clean interface and enhanced electrostatic control, which helps reveal the intrinsic ferroelectric properties of the $3R$-$\mathrm{MoS_2}$ channel.

B. Structural characterization

Second-harmonic generation (SHG) mapping and x-ray diffraction (XRD) measurements were performed to characterize the structural properties of the $3R$-$\mathrm{MoS_2}$ sample. SHG signals were acquired using a spectrometer coupled to a 50× objective lens ($\mathrm{NA} = 0.62$) under picosecond-pulsed laser excitation at a wavelength of 1240 nm. Spatially resolved SHG mapping was recorded over the designated area. XRD patterns were collected on a PANalytical Empyrean diffractometer using monochromatic Cu Kα

radiation ($\lambda = 1.5406$ Å), with a 2θ scan range of 5°–80° and a scanning speed of 2°/ min.

Scanning tunneling microscopy (STM) investigations were carried out using an RHK-Tech PanScan Freedom STM setup at low temperature (9 K) under UHV conditions (10^{-11} mbar) on a bulk $3R$-$\mathrm{MoS_2}$ crystal exfoliated onto an Au(111) surface by gold-assisted exfoliation.

C. Computational modeling

1. Density functional theory

All density-functional-theory (DFT) calculations are performed using the Vienna *ab initio* simulation package [66,67]. The exchange-correlation interaction is treated with the Perdew-Burke-Ernzerhof functional [68] augmented with Grimme's D3 dispersion correction with the Becke-Johnson damping function [69]. Electron-ion interactions are described using the projector-augmented-wave method [70]. A plane-wave kinetic energy cutoff of 500 eV is employed, and the KSPACING tag is set to 0.25 Å^{-1} for k-point sampling in the Brillouin zone. A vacuum region of more than 20 Å thick is included to avoid interactions between periodic images. The minimum energy pathways are determined using the climbing-image nudged-elastic-band approach [71]. Additionally, the dipole correction scheme proposed by Neugebauer and Scheffler [72] is incorporated throughout.

2. DPMD

The DPMD simulations of the rhombohedral-stacked $\mathrm{MoS_2}$ are performed using a DP model [73] trained on data from first-principles DFT calculations. The smooth edition (DeepPot-SE) is employed to describe the potential energy surface [74], while the DP-GEN protocol [75,76] is used to sample structures for model training (see Supplemental Material Fig. S1 for details [29]). A compact deep neural-network architecture is adopted to enable efficient large-scale MD simulations. Additionally, a model compression technique [77] is used to further enhance computational efficiency. To assess the accuracy of our model, we compare the DP and DFT results on a training dataset consisting of 3371 configurations for force and energy predictions, and validate the model's accuracy in predicting dynamic properties, including the phonon spectrum, the biaxial strain effect, the unit-cell polarization switching barrier, and the energy evolution along an MD trajectory at 300 K; see details in Supplemental Material Figs. S2 and S3 [29]. In all cases, the model exhibited high accuracy, particularly in simulating the polarization switching process in the $\mathrm{MoS_2}$ bilayer.

D. KPFM measurements

The surface potential was characterized using the Asylum Research Cypher S operating in KPFM mode with an HQ:NSC14/Cr-Au conductive probe. KPFM incorporates an additional feedback loop to detect changes in the sample's surface potential. During the first pass, the system operates similarly to conventional ac mode, capturing the sample's topography. In the subsequent pass, the probe is lifted to a fixed height above the surface, allowing measurement of the potential difference between the probe tip and the sample. In addition, the sample was placed on a thin graphite flake that served as a conductive bottom electrode, electrically connected to a predeposited contact to ensure effective grounding.

E. Electrical measurements

All electrical measurements were performed using an FS-Pro 380 semiconductor parameter analyzer in a vacuum chamber at 10^{-2} Torr. For all dual-gate measurements, the voltages on the symmetric gates (top gate V_{TG}, bottom gate V_{BG}) were regulated according to the expression $V_{\mathrm{BG}} = -\alpha V_{\mathrm{TG}}$ (where $\alpha = d_b/d_t$, and d_t and d_b are the thickness of the bottom and top h-BN dielectric layers) to avoid net carrier doping in the channel. All the pulse switching measurements were conducted using the built-in pulse measurement functions of the analyzer, in which a pair of top and bottom gate pulses V_{TG}-V_{BG} was simultaneously applied to apply the electric field with negligible doping effect. For simplicity, while the V_{TG}-V_{BG} paired voltages are applied, only the details of applied V_{TG} are described in each measurement in the main text.

1. Dynamic electrical measurements

For the dynamic electrical measurements, a continuous V_{TG}-V_{BG} is applied. The amplitude of V_{TG} sweeps from −3 to 3 V in 0.05 V increments (upward sweep), then from 3 V back to −3 V in 0.05 V decrements (downward sweep).

2. Static electrical measurements

For the static electrical measurements, V_{TG}-V_{BG} is encoded as a series of electrical pulses with a period of 0.02 s. The amplitude of V_{TG} varies from −3 to 3 V in 0.1 V steps, then back to −3 V in −0.1 V steps (see Supplemental Material Fig. S13 [29]). The drain current is recorded after each V_{TG}-V_{BG} pulse stimulus using a fixed pulse with a period of 0.02 s and an amplitude of −0.12 V.

3. Sequential scanning measurements

Sequential scanning measurements are characterized by sequentially applying $V_{\mathrm{TG}}^{\mathrm{set}}$ or $V_{\mathrm{TG}}^{\mathrm{reset}}$ in amplitude order (see Supplemental Material Fig. S16 [29]), with repeated forward and backward scanning. In the forward mode, a fixed revert V_{TG} ($V_{\mathrm{TG}}^{\mathrm{revert}}$) of −3 V was applied, followed by a varying set V_{TG} pulse ($V_{\mathrm{TG}}^{\mathrm{set}}$) that ranged from 1.64 to 3.14 V in increments of 0.1 V. In the backward mode, a fixed $V_{\mathrm{TG}}^{\mathrm{revert}}$ of 3.1 V was applied, followed by a varying reset V_{TG} pulse ($V_{\mathrm{TG}}^{\mathrm{reset}}$) that ranged from −1 to −3 V in decrements of −0.1 V.

In both modes, the drain current after each pulsed electric-field excitation was recorded by the fixed drain-source voltage pulse ($V_{\mathrm{DS}}^{\mathrm{read}}$) with an amplitude of −0.1 V.

4. Iterative scanning measurements

Iterative scanning measurements are characterized by the alternate application of $V_{\mathrm{TG}}^{\mathrm{set}}$ and $V_{\mathrm{TG}}^{\mathrm{reset}}$ (see Supplemental Material Fig. S18 [29]), with repeated forward and backward scanning. In the forward mode, within the same group, a fixed revert V_{TG} ($V_{\mathrm{TG}}^{\mathrm{revert}}$) of 3.1 V was applied, followed by an alternating pulse sequence consisting of a fixed reset V_{TG} pulse ($V_{\mathrm{TG}}^{\mathrm{reset}}$) and a set V_{TG} pulse ($V_{\mathrm{TG}}^{\mathrm{set}}$) that varied from 1.64 to 3.14 V in steps of 0.1 V. Across different groups, $V_{\mathrm{TG}}^{\mathrm{reset}}$ was varied from −1 to −3 V in steps of −0.1 V.

In the backward mode, within the same group, a fixed $V_{\mathrm{TG}}^{\mathrm{revert}}$ of −3 V was applied, followed by an alternating pulse sequence consisting of a fixed $V_{\mathrm{TG}}^{\mathrm{set}}$ pulse and a $V_{\mathrm{TG}}^{\mathrm{reset}}$ pulse that varied from −1 to −3 V in steps of −0.1 V. Across different groups, $V_{\mathrm{TG}}^{\mathrm{set}}$ was varied from 1.64 to 3.14 V in steps of 0.1 V.

In both modes, the drain current after each pulsed electric-field excitation was recorded by the fixed drain-source voltage pulse ($V_{\mathrm{DS}}^{\mathrm{read}}$) with an amplitude of −0.1 V.

ACKNOWLEDGMENTS

The authors appreciate W. Ren and A. Zhou from the Analysis and Testing Center, University of Electronic Science and Technology of China, for technical support. This work was supported by the National Natural Science Foundation of China (Grant No. 92477115), the Scientific Research Innovation Capability Support Project for Young Faculty (Grant No. ZYGXQNJSKYCXNLZCXM-I7), the National Key Research & Development Program (Grant No. 2020YFA0309200), the National Natural Science Foundation of China (Grant No. 62274024), Sichuan Science and Technology Program (Grant No. 2025ZYD0182), Natural Science Foundation of China (Grant No. 12304128), Zhejiang Provincial Natural Science Foundation of China (Grant No. LR25A040004), and Sichuan Province Key Laboratory of Display Science and Technology. The computational resource is provided by the Open Source Supercomputing Center of S-A-I and Westlake HPC Center.

F. L. supervised the project. F. L., J. C., S. L., and X. L. conceived the idea. J. C. and R. B. fabricated the dual-gate field-effect transistor, performed the electronic-transport measurements, and analyzed the data, and with the assistance of F. Y. and B. D., E. P. performed the KPFM characterization. C. K. and S. L. performed the molecular dynamics simulations. Z. L. and Q. L. synthesized the $3R$-MoS$_2$ crystal. L. T. and P. K. performed the STM investigations. X. L., Q. L., F. L., and S. L. analyzed the data. J. C., C. K., R. B., S. L., and F. L. wrote the manuscript with input from all the authors. All authors discussed the results.

The authors declare no competing interests.

DATA AVAILABILITY

The data supporting this study's findings are available within the article.

[1] V. K. Sangwan, H.-S. Lee, H. Bergeron, I. Balla, M. E. Beck, K.-S. Chen, and M. C. Hersam, *Multi-terminal memtransistors from polycrystalline monolayer molybdenum disulfide*, Nature (London) **554**, 500 (2018).

[2] E. J. Fuller, S. T. Keene, A. Melianas, Z. Wang, S. Agarwal, Y. Li, Y. Tuchman, C. D. James, M. J. Marinella, and J. J. Yang, *Parallel programming of an ionic floating-gate memory array for scalable neuromorphic computing*, Science **364**, 570 (2019).

[3] K. Ding, J. Wang, Y. Zhou, H. Tian, L. Lu, R. Mazzarello, C. Jia, W. Zhang, F. Rao, and E. Ma, *Phase-change heterostructure enables ultralow noise and drift for memory operation*, Science **366**, 210 (2019).

[4] H. Ning, Z. Yu, Q. Zhang, H. Wen, B. Gao, Y. Mao, Y. Li, Y. Zhou, Y. Zhou, and J. Chen, *An in-memory computing architecture based on a duplex two-dimensional material structure for in situ machine learning*, Nat. Nanotechnol. **18**, 493 (2023).

[5] Y. H. Shin, I. Grinberg, I. W. Chen, and A. M. Rappe, *Nucleation and growth mechanism of ferroelectric domain-wall motion*, Nature (London) **449**, 881 (2007).

[6] J. Y. Jo, D. J. Kim, Y. S. Kim, S. B. Choe, T. K. Song, J. G. Yoon, and T. W. Noh, *Polarization switching dynamics governed by the thermodynamic nucleation process in ultrathin ferroelectric films*, Phys. Rev. Lett. **97**, 247602 (2006).

[7] K. M. Rabe, C. H. Ahn, and J.-M. Triscone, *Physics of Ferroelectrics: A Modern Perspective* (Springer Science & Business Media, Berlin, 2007), Vol. 105.

[8] J. E. Zhou, T.-L. Cheng, and Y. U. Wang, *Correlated nucleation and self-accommodating kinetic pathway of ferroelectric phase transformation*, J. Appl. Phys. **111**, 024105 (2012).

[9] S. Liu, I. Grinberg, and A. M. Rappe, *Intrinsic ferroelectric switching from first principles*, Nature (London) **534**, 360 (2016).

[10] Y. Ishibashi and Y. Takagi, *Note on ferroelectric domain switching*, J. Phys. Soc. Jpn. **31**, 506 (1971).

[11] Y. A. Genenko, S. Zhukov, S. V. Yampolskii, J. Schütrumpf, R. Dittmer, W. Jo, H. Kungl, M. J. Hoffmann, and H. von Seggern, *Universal polarization switching behavior of disordered ferroelectrics*, Adv. Funct. Mater. **22**, 2058 (2012).

[12] J. Y. Jo, H. S. Han, J. G. Yoon, T. K. Song, S. H. Kim, and T. W. Noh, *Domain switching kinetics in disordered ferroelectric thin films*, Phys. Rev. Lett. **99**, 267602 (2007).

[13] H. Mulaosmanovic, J. Ocker, S. Müller, U. Schroeder, J. Müller, P. Polakowski, S. Flachowsky, R. van Bentum, T. Mikolajick, and S. Slesazeck, *Switching kinetics in nanoscale hafnium oxide based ferroelectric field-effect transistors*, ACS Appl. Mater. Interfaces **9**, 3792 (2017).

[14] S. Jesse, B. J. Rodriguez, S. Choudhury, A. P. Baddorf, I. Vrejoiu, D. Hesse, M. Alexe, E. A. Eliseev, A. N. Morozovska, J. Zhang, L. Q. Chen, and S. V. Kalinin, *Direct imaging of the spatial and energy distribution of nucleation centres in ferroelectric materials*, Nat. Mater. **7**, 209 (2008).

[15] P. Gao, C. T. Nelson, J. R. Jokisaari, S. H. Baek, C. W. Bark, Y. Zhang, E. Wang, D. G. Schlom, C. B. Eom, and X. Pan, *Revealing the role of defects in ferroelectric switching with atomic resolution*, Nat. Commun. **2**, 591 (2011).

[16] P. Gao, J. Britson, J. R. Jokisaari, C. T. Nelson, S.-H. Baek, Y. Wang, C.-B. Eom, L.-Q. Chen, and X. Pan, *Atomic-scale mechanisms of ferroelastic domain-wall-mediated ferroelectric switching*, Nat. Commun. **4**, 2791 (2013).

[17] K. Ni, J. Smith, H. Ye, B. Grisafe, G. B. Rayner, A. Kummel, and S. Datta, *A novel ferroelectric superlattice based multilevel cell non-volatile memory*, in *Proceedings of the 2019 IEEE International Electron Devices Meeting (IEDM) 28.8.1* (IEEE, New York, 2019), 10.1109/IEDM19573.2019.8993670.

[18] M. Vizner Stern, Y. Waschitz, W. Cao, I. Nevo, K. Watanabe, T. Taniguchi, E. Sela, M. Urbakh, O. Hod, and M. Ben Shalom, *Interfacial ferroelectricity by van der Waals sliding*, Science **372**, 1462 (2021).

[19] X. Wang, K. Yasuda, Y. Zhang, S. Liu, K. Watanabe, T. Taniguchi, J. Hone, L. Fu, and P. Jarillo-Herrero, *Interfacial ferroelectricity in rhombohedral-stacked bilayer transition metal dichalcogenides*, Nat. Nanotechnol. **17**, 367 (2022).

[20] A. Jindal, A. Saha, Z. Li, T. Taniguchi, K. Watanabe, J. C. Hone, T. Birol, R. M. Fernandes, C. R. Dean, A. N. Pasupathy, and D. A. Rhodes, *Coupled ferroelectricity and superconductivity in bilayer* T_d-$MoTe_2$, Nature (London) **613**, 48 (2023).

[21] F. Sui, M. Jin, Y. Zhang, R. Qi, Y.-N. Wu, R. Huang, F. Yue, and J. Chu, *Sliding ferroelectricity in van der Waals layered* $\gamma-$InSe *semiconductor*, Nat. Commun. **14**, 36 (2023).

[22] A. Weston, E. G. Castanon, V. Enaldiev, F. Ferreira, S. Bhattacharjee, S. Xu, H. Corte-León, Z. Wu, N. Clark, and A. Summerfield, *Interfacial ferroelectricity in marginally twisted 2D semiconductors*, Nat. Nanotechnol. **17**, 390 (2022).

[23] L. Rogée, L. Wang, Y. Zhang, S. Cai, P. Wang, M. Chhowalla, W. Ji, and S. P. Lau, *Ferroelectricity in untwisted heterobilayers of transition metal dichalcogenides*, Science **376**, 973 (2022).

[24] P. Meng, Y. Wu, R. Bian, E. Pan, B. Dong, X. Zhao, J. Chen, L. Wu, Y. Sun, Q. Fu, Q. Liu, D. Shi, Q. Zhang, Y.-W. Zhang, Z. Liu, and F. Liu, *Sliding induced multiple polarization states in two-dimensional ferroelectrics*, Nat. Commun. **13**, 7696 (2022).

[25] M. Wu and J. Li, *Sliding ferroelectricity in 2D van der Waals materials: Related physics and future opportunities*, Proc. Natl. Acad. Sci. U.S.A. **118**, e2115703118 (2021).

[26] P. Tang and Gerrit E. W. Bauer, *Sliding phase transition in ferroelectric van der Waals bilayers*, Phys. Rev. Lett. **130**, 176801 (2023).

[27] F. Liu, L. You, K. L. Seyler, X. Li, P. Yu, J. Lin, X. Wang, J. Zhou, H. Wang, H. He, S. T. Pantelides, W. Zhou, P. Sharma, X. Xu, P. M. Ajayan, J. Wang, and Z. Liu, *Room-temperature ferroelectricity in* $CuInP_2S_6$ *ultrathin flakes*, Nat. Commun. **7**, 12357 (2016).

[28] F. Xue, W. Hu, K. C. Lee, L. S. Lu, J. Zhang, H. L. Tang, A. Han, W. T. Hsu, S. Tu, W. H. Chang, C. H. Lien, J. H. He, Z. Zhang, L. J. Li, and X. Zhang, *Room-temperature ferroelectricity in hexagonally layered* $\alpha-In_2Se_3$ *nanoflakes down to the monolayer limit*, Adv. Funct. Mater. **28**, 1803738 (2018).

[29] See Supplemental Material at http://link.aps.org/supplemental/10.1103/q624-x397 for more details on the molecular dynamics simulations and the electrical measurement results, which includes Refs. [19,24,30,31].

[30] A. Di Bartolomeo, A. Grillo, F. Urban, L. Iemmo, F. Giubileo, G. Luongo, G. Amato, L. Croin, L. Sun, S.-J. Liang, and L. K. Ang, *Asymmetric Schottky contacts in bilayer* MoS_2 *field effect transistors*, Adv. Funct. Mater. **28**, 1800657 (2018).

[31] Y. A. Eshete, K. Kang, S. Kang, Y. Kim, P. L. Nguyen, D. Y. Cho, Y. Kim, J. Lee, S. Cho, and H. Yang, *Atomic and electronic manipulation of robust ferroelectric polymorphs*, Adv. Mater. **34**, e2202633 (2022).

[32] K. Ko, A. Yuk, R. Engelke, S. Carr, J. Kim, D. Park, H. Heo, H. M. Kim, S. G. Kim, H. Kim, T. Taniguchi, K. Watanabe, H. Park, E. Kaxiras, S. M. Yang, P. Kim, and H. Yoo, *Operando electron microscopy investigation of polar domain dynamics in twisted van der Waals homobilayers*, Nat. Mater. **22**, 992 (2023).

[33] E. Y. Tsymbal, *Two-dimensional ferroelectricity by design*, Science **372**, 1389 (2021).

[34] L. Jiang, S. Wang, Z. Shi, C. Jin, M. I. B. Utama, S. Zhao, Y. R. Shen, H. J. Gao, G. Zhang, and F. Wang, *Manipulation of domain-wall solitons in bi-and trilayer graphene*, Nat. Nanotechnol. **13**, 204 (2018).

[35] V. Y. Shur, E. Rumyantsev, V. Kuminov, A. Subbotin, and V. Kozhevnikov, *Barkhausen effect in stepped motion of a plane domain boundary in gadolinium molybdate*, Phys. Solid State **41**, 269 (1999).

[36] D. Kim, J. Jo, T. Kim, S. Yang, B. Chen, Y. Kim, and T. Noh, *Observation of inhomogeneous domain nucleation in epitaxial* $Pb(Zr,Ti)O_3$ *capacitors*, Appl. Phys. Lett. **91**, 132903 (2007).

[37] L. Li, L. Xie, and X. Pan, *Real-time studies of ferroelectric domain switching: A review*, Rep. Prog. Phys. **82**, 126502 (2019).

[38] R. Diaz Pardo, W. Savero Torres, A. B. Kolton, S. Bustingorry, and V. Jeudy, *Universal depinning transition of domain walls in ultrathin ferromagnets*, Phys. Rev. B **95**, 184434 (2017).

[39] S. Park, D. Lee, J. Kang, H. Choi, and J. H. Park, *Laterally gated ferroelectric field effect transistor (LG-FeFET) using*

alpha-In_2Se_3 *for stacked in-memory computing array*, Nat. Commun. **14**, 6778 (2023).

[40] I. J. Kim, M. K. Kim, and J. S. Lee, *Highly-scaled and fully-integrated 3-dimensional ferroelectric transistor array for hardware implementation of neural networks*, Nat. Commun. **14**, 504 (2023).

[41] G. Feng *et al.*, *A ferroelectric fin diode for robust non-volatile memory*, Nat. Commun. **15**, 513 (2024).

[42] X. Mou, J. Tang, Y. Lyu, Q. Zhang, S. Yang, F. Xu, W. Liu, M. Xu, Y. Zhou, and W. Sun, *Analog memristive synapse based on topotactic phase transition for high-performance neuromorphic computing and neural network pruning*, Sci. Adv. **7**, eabh0648 (2021).

[43] Z. Gao, Y. Wang, Z. Lv, P. Xie, Z.-X. Xu, M. Luo, Y. Zhang, S. Huang, K. Zhou, G. Zhang, G. Duan, Y. Zhou, and S.-T. Han, *Ferroelectric coupling for dual-mode non-filamentary memristors*, Appl. Phys. Rev. **9**, 021417 (2022).

[44] R. Cao, X. Zhang, S. Liu, J. Lu, Y. Wang, H. Jiang, Y. Yang, Y. Sun, W. Wei, J. Wang, H. Xu, Q. Li, and Q. Liu, *Compact artificial neuron based on anti-ferroelectric transistor*, Nat. Commun. **13**, 7018 (2022).

[45] A. Q. Jiang, W. P. Geng, P. Lv, J. W. Hong, J. Jiang, C. Wang, X. J. Chai, J. W. Lian, Y. Zhang, R. Huang, D. W. Zhang, J. F. Scott, and C. S. Hwang, *Ferroelectric domain wall memory with embedded selector realized in* $LiNbO_3$ *single crystals integrated on Si wafers*, Nat. Mater. **19**, 1188 (2020).

[46] Q. Li, S. Wang, Z. Li, X. Hu, Y. Liu, J. Yu, Y. Yang, T. Wang, J. Meng, Q. Sun, D. W. Zhang, and L. Chen, *High-performance ferroelectric field-effect transistors with ultra-thin indium tin oxide channels for flexible and transparent electronics*, Nat. Commun. **15**, 2686 (2024).

[47] Y. Jia, Q. Yang, Y. W. Fang, Y. Lu, M. Xie, J. Wei, J. Tian, L. Zhang, and R. Yang, *Giant tunnelling electroresistance in atomic-scale ferroelectric tunnel junctions*, Nat. Commun. **15**, 693 (2024).

[48] M. K. Kim, I. J. Kim, and J. S. Lee, *CMOS-compatible compute-in-memory accelerators based on integrated ferroelectric synaptic arrays for convolution neural networks*, Sci. Adv. **8**, eabm8537 (2022).

[49] J. Li, C. Ge, J. Du, C. Wang, G. Yang, and K. Jin, *Reproducible ultrathin ferroelectric domain switching for high-performance neuromorphic computing*, Adv. Mater. **32**, e1905764 (2020).

[50] Z. Luo, Z. Wang, Z. Guan, C. Ma, L. Zhao, C. Liu, H. Sun, H. Wang, Y. Lin, X. Jin, Y. Yin, and X. Li, *High-precision and linear weight updates by subnanosecond pulses in ferroelectric tunnel junction for neuro-inspired computing*, Nat. Commun. **13**, 699 (2022).

[51] J. Jiang, Z. L. Bai, Z. H. Chen, L. He, D. W. Zhang, Q. H. Zhang, J. A. Shi, M. H. Park, J. F. Scott, C. S. Hwang, and A. Q. Jiang, *Temporary formation of highly conducting domain walls for non-destructive read-out of ferroelectric domain-wall resistance switching memories*, Nat. Mater. **17**, 49 (2018).

[52] P. Sharma, Q. Zhang, D. Sando, C. H. Lei, Y. Liu, J. Li, V. Nagarajan, and J. Seidel, *Nonvolatile ferroelectric domain wall memory*, Sci. Adv. **3**, e1700512 (2017).

[53] K. H. Kim *et al.*, *Scalable CMOS back-end-of-line-compatible* AlScN/*two-dimensional channel ferroelectric field-effect transistors*, Nat. Nanotechnol. **18**, 1044 (2023).

[54] Y. Zhou, Y. Wang, F. Zhuge, J. Guo, S. Ma, J. Wang, Z. Tang, Y. Li, X. Miao, Y. He, and Y. Chai, *A reconfigurable two*-WSe_2-*transistor synaptic cell for reinforcement learning*, Adv. Mater. **34**, 2107754 (2022).

[55] S. Wang, L. Liu, L. Gan, H. Chen, X. Hou, Y. Ding, S. Ma, D. W. Zhang, and P. Zhou, *Two-dimensional ferroelectric channel transistors integrating ultra-fast memory and neural computing*, Nat. Commun. **12**, 53 (2021).

[56] J. Wu, H.-Y. Chen, N. Yang, J. Cao, X. Yan, F. Liu, Q. Sun, X. Ling, J. Guo, and H. Wang, *High tunnelling electroresistance in a ferroelectric van der Waals heterojunction via giant barrier height modulation*, Nat. Electron. **3**, 466 (2020).

[57] X. Yan, Z. Zheng, V. K. Sangwan, J. H. Qian, X. Wang, S. E. Liu, K. Watanabe, T. Taniguchi, S. Y. Xu, P. Jarillo-Herrero, Q. Ma, and M. C. Hersam, *Moire synaptic transistor with room-temperature neuromorphic functionality*, Nature (London) **624**, 551 (2023).

[58] C. Ma, Z. Luo, W. Huang, L. Zhao, Q. Chen, Y. Lin, X. Liu, Z. Chen, C. Liu, H. Sun, X. Jin, Y. Yin, and X. Li, *Sub-nanosecond memristor based on ferroelectric tunnel junction*, Nat. Commun. **11**, 1439 (2020).

[59] R. Xu, S. Liu, S. Saremi, R. Gao, J. J. Wang, Z. Hong, H. Lu, A. Ghosh, S. Pandya, E. Bonturim, Z. H. Chen, L. Q. Chen, A. M. Rappe, and L. W. Martin, *Kinetic control of tunable multi-state switching in ferroelectric thin films*, Nat. Commun. **10**, 1282 (2019).

[60] D. T. Ahneman, J. G. Estrada, S. Lin, S. D. Dreher, and A. G. Doyle, *Predicting reaction performance in* $C-N$ *cross-coupling using machine learning*, Science **360**, 186 (2018).

[61] T. Dalgaty, N. Castellani, C. Turck, K.-E. Harabi, D. Querlioz, and E. Vianello, *In situ learning using intrinsic memristor variability via Markov chain Monte Carlo sampling*, Nat. Electron. **4**, 151 (2021).

[62] S. Forrest, *Genetic algorithms: Principles of natural selection applied to computation*, Science **261**, 872 (1993).

[63] K.-E. Harabi, T. Hirtzlin, C. Turck, E. Vianello, R. Laurent, J. Droulez, P. Bessière, J.-M. Portal, M. Bocquet, and D. Querlioz, *A memristor-based Bayesian machine*, Nat. Electron. **6**, 52 (2023).

[64] W. Li and M. Alexe, *Investigation on switching kinetics in epitaxial* $Pb(Zr_{0.2}Ti_{0.8})O_3$ *ferroelectric thin films: Role of the 90 domain walls*, Appl. Phys. Lett. **91**, 262903 (2007).

[65] P. Behera, A. M. Ross, N. Shanker, P. Meisenheimer, M. Manna, C. C. Lin, S. L. Hsu, I. Harris, P. Kavle, and S. Husain, *Anisotropic ferroelectricity in polar vortices*, Adv. Mater. **37**, 2410149 (2025).

[66] G. Kresse and J. Furthmüller, *Efficient iterative schemes for ab initio total-energy calculations using a plane-wave basis set*, Phys. Rev. B **54**, 11169 (1996).

[67] G. Kresse and J. Furthmüller, *Efficiency of ab-initio total energy calculations for metals and semiconductors using a plane-wave basis set*, Comput. Mater. Sci. **6**, 15 (1996).

[68] J. P. Perdew, K. Burke, and M. Ernzerhof, *Generalized gradient approximation made simple*, Phys. Rev. Lett. **77**, 3865 (1996).

[69] S. Grimme, S. Ehrlich, and L. Goerigk, *Effect of the damping function in dispersion corrected density functional theory*, J. Comput. Chem. **32**, 1456 (2011).

[70] P. E. Blöchl, *Projector augmented-wave method*, Phys. Rev. B **50**, 17953 (1994).

[71] G. Henkelman, B. P. Uberuaga, and H. Jónsson, *A climbing image nudged elastic band method for finding saddle points and minimum energy paths*, J. Chem. Phys. **113**, 9901 (2000).

[72] J. Neugebauer and M. Scheffler, *Adsorbate-substrate and adsorbate-adsorbate interactions of* Na *and* K *adlayers on* Al(111), Phys. Rev. B **46**, 16067 (1992).

[73] H. Wang, L. Zhang, J. Han, and E. Weinan, *DeePMD-kit: A deep learning package for many-body potential energy representation and molecular dynamics*, Comput. Phys. Commun. **228**, 178 (2018).

[74] L. Zhang, J. Han, H. Wang, W. Saidi, and R. Car, *End-to-end symmetry preserving inter-atomic potential energy model for finite and extended systems*, Adv. Neural Inf. Process. Syst. **31**, 4436 (2018).

[75] Y. Zhang, H. Wang, W. Chen, J. Zeng, L. Zhang, H. Wang, and E. Weinan, *DP-GEN: A concurrent learning platform for the generation of reliable deep learning based potential energy models*, Comput. Phys. Commun. **253**, 107206 (2020).

[76] L. Zhang, D.-Y. Lin, H. Wang, R. Car, and W. E, *Active learning of uniformly accurate interatomic potentials for materials simulation*, Phys. Rev. Mater. **3**, 023804 (2019).

[77] J. Zeng, D. Zhang, D. Lu, P. Mo, Z. Li, Y. Chen, M. Rynik, L. a. Huang, Z. Li, and S. Shi, *DeePMD-kit v2: A software package for deep potential models*, J. Chem. Phys. **159**, 054801 (2023).